Fully kinetic simulations of undriven magnetic reconnection with open boundary conditions

William Daughton[a] and Jack Scudder
Department of Physics and Astronomy, University of Iowa, Iowa City, Iowa 52242

Homa Karimabadi
Department of Electrical and Computer Engineering, University of California, San Diego, La Jolla, California 92093

(Received 15 May 2006; accepted 7 June 2006; published online 12 July 2006)

Kinetic simulations of magnetic reconnection typically employ periodic boundary conditions that limit the duration in which the results are physically meaningful. To address this issue, a new model is proposed that is open with respect to particles, magnetic flux, and electromagnetic radiation. The model is used to examine undriven reconnection in a neutral sheet initialized with a single x-point. While at early times the results are in excellent agreement with previous periodic studies, the evolution over longer intervals is entirely different. In particular, the length of the electron diffusion region is observed to increase with time resulting in the formation of an extended electron current sheet. As a consequence, the electron diffusion region forms a bottleneck and the reconnection rate is substantially reduced. Periodically, the electron layer becomes unstable and produces a secondary island, breaking the diffusion region into two shorter segments. After growing for some period, the island is ejected and the diffusion region again expands until a new island is formed. Fast reconnection may still be possible provided that the generation of secondary islands remains sufficiently robust. These results indicate that reconnection in a neutral sheet may be inherently unsteady and raise serious questions regarding the standard model of Hall mediated reconnection. [DOI: 10.1063/1.2218817]

I. INTRODUCTION

Collisionless magnetic reconnection is a basic plasma process in which magnetic field energy is rapidly converted into kinetic energy.[1] Understanding this process is of fundamental importance to a variety of applications including planetary magnetospheres,[2] solar flares, laboratory fusion machines, and astrophysical plasmas. Despite considerable progress, many basic questions regarding collisionless reconnection remain poorly understood.

In the study of magnetic reconnection, it is important to distinguish between *undriven* and *driven* reconnection. In the undriven case, reconnection is allowed to develop from the pre-existing gradients within the system while in the driven case an external inflow forces plasma and magnetic flux into the system in a prescribed manner. Most theoretical models have focused on 2D steady state reconnection in the presence of a single x-line. In this limit, resistive magnetohydrodynamics (MHD) simulations have established a direct link between the length of the diffusion region and the type of reconnection possible.[3–8] Within the MHD model, the length of the diffusion region is determined by the localization scale of the resistivity. A continuum of solutions are obtained ranging from fast reconnection (e.g., Petschek regime) when resistivity is localized to inefficient reconnection (e.g., Sweet-Parker regime) when resistivity is uniform.

Efforts to explain fast reconnection in collisionless plasmas have thus focused on identifying physical processes that may localize the diffusion region. In a kinetic plasma, the structure of the diffusion region is thought to consists of an inner electron region and an outer ion region as illustrated in Fig. 1. The question then arises as to the physical extent, stability, and relative role of each diffusion region in controlling reconnection. Since there is no first-principles theory to address these fundamental questions, simulations and scaling arguments have played a prominent role.[8–15] From these efforts, a widely accepted model has emerged that places considerable emphasis on the importance of the Hall physics to explain fast reconnection. Although the Hall term does not contribute to the parallel electric field, it is thought to facilitate reconnection in two ways. First, the dispersive properties of whistler waves permit the flux of electrons through the inner diffusion region to remain finite, even as the dissipation approaches zero. As a consequence, the electrons do not limit the reconnection rate, provided that the length of the electron diffusion region D_e remains microscopic. Instead, the reconnection rate is controlled by the ion diffusion region which has a width δ_i on the order of the ion inertial length $d_i = c/\omega_{pi}$. Furthermore, it is argued that Hall physics is also responsible for localizing the length D_i of the ion diffusion region to permit fast reconnection.[8,12,13,15] In the GEM study,[14] it was found that all simulations that included the Hall term obtained similar fast reconnection rates. While some researchers have concluded that the Hall mediated reconnection rate is independent of the system size,[12,15,16] others have found a significant dependence.[17,18]

Follow up studies have raised a number of questions regarding the role of the Hall physics in kinetic simulations.

[a]Electronic mail: william-daughton@uiowa.edu

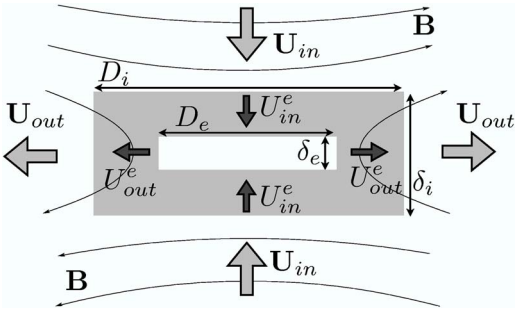

FIG. 1. Idealized structure of the diffusion region in a kinetic plasma. Ions are unmagnetized within the grey region while electrons are unmagnetized in the inner white region.

In particular, hybrid simulations (kinetic ions, fluid electrons) in which the Hall term is intentionally removed have found similar reconnection rates.[19] While in fluid theory the Hall term is required to obtain fast reconnection, it appears that in a kinetic plasma the role of Hall term is muted and ion kinetic effects can still permit fast reconnection. In addition, it is well-known that fast reconnection can still exists in the limit of $m_i = m_e$ where the Hall term cancels and whistler waves are absent.[20]

Another important issue is the stability of the diffusion region which may determine if reconnection is quasisteady or intermittent. For a single x-line, MHD simulations indicate the diffusion region is stable when the resistivity is localized,[5,21] while a uniform resistivity gives rise to a Sweet-Parker layer which can in turn become unstable to secondary tearing.[4,5,21–23] Within two-fluid models, a single x-line is thought to be stable with a reconnection rate highly insensitive to the dissipation mechanism. This result has been demonstrated in large two-fluid simulations with periodic boundary conditions[12,15] and also using Hall MHD with open boundary conditions.[16] In these open boundary simulations, the Hall electric field asymptotes to a maximum value and does not decrease in time. Hybrid simulations have also reported a stable x-line configuration[24–26] but a recent study indicates the possibility of stretching of the diffusion region and intermittent reconnection.[27] Fully kinetic particle-in-cell (PIC) simulations of driven reconnection have observed secondary island formation depending on the profile of the driving electric field.[28] However, full PIC simulations of undriven reconnection[27,29–32] have found no evidence for secondary island formation, but these results were limited by small system size and periodic boundary conditions.

Although fully kinetic PIC simulations offer a first-principles approach to evaluate the structure and stability of the diffusion region, the widespread use of periodic boundary conditions limits the physical relevance of the results. To properly model the diffusion region, the simulation domain must be sufficiently large to prevent the artificial recirculation of particles and magnetic flux during the time interval of interest. This is very difficult to achieve with full PIC and thus the results are only physically meaningful for the relatively short period of time before the reconnection jets collide. While this issue is also a concern in fluid simulations, the problem is even more severe with full PIC due to the intense electron flows generated along the separatrices that can easily exceed the electron thermal speed. These flows are rapidly recirculated through the system along the separatrices and back to the diffusion region, potentially influencing the dynamics even before the reconnection jets collide. Thus issues related to the basic structure and stability of the diffusion region and the separatrices cannot be properly addressed using periodic boundary conditions.

To make progress, it is crucial to develop appropriate open boundary conditions for full PIC simulations. In choosing these boundary conditions, the goal is to effectively mimic a much larger system than is otherwise possible. Various types of open boundary conditions have been implemented in MHD,[21] Hall MHD,[16,33] and hybrid.[19,34,35] However, the implementation of open boundary conditions is more difficult in full PIC due to a variety of factors including the presence of high frequency waves and the requirement for an additional electrostatic boundary condition. The few researchers who have made attempts focused entirely on driven reconnection in which the electric field is specified on the inflow boundary while a variety of conditions are specified on the outflow boundary.[36–42] For the case of undriven reconnection, it does not appear that any researchers have implemented open boundary conditions for full PIC.

In this work, a new open boundary model is described for full PIC simulations of magnetic reconnection. The inflow and outflow boundaries are treated symmetrically and are open with respect to particles, magnetic flux and electromagnetic radiation. These boundary conditions do not correspond to any physical boundary, but are chosen to truncate the computational domain and mimic a larger system. The approach relies on three main innovations:

1. A technique to inject particles from the boundary in a way that approximately enforces a zero normal derivative condition on the moments up through the full pressure tensor.
2. An electrostatic boundary condition that permits electrostatic structures to extend smoothly to the outflow boundary.
3. An electromagnetic boundary condition that permits electromagnetic radiation to leave the system, while approximately enforcing a zero normal derivative condition on the magnetic field.

While the model has been tested for a range of guide fields, this manuscript focuses on reconnection in a neutral sheet. In this limit, comparisons with much larger periodic simulations provide strong evidence indicating the new model can indeed mimic a larger system.

The new open boundary conditions permit the diffusion region to develop over time scales much longer than have ever been simulated with a fully kinetic approach. During the initial phase, the evolution of the system and the observed reconnection rates are in excellent agreement with a large body of previous work. However, over longer time periods, the structure of the diffusion region continues to evolve and the results are dramatically different. Indeed, these results require a re-examination of the standard model of Hall me-

diated reconnection. In particular, the length of the electron diffusion region does not remain microscopic, but expands in time to $D_e \sim 25d_i$ for the case considered. As a result, the reconnection rate drops and a spatially extended electron current sheet is formed in the diffusion region. Periodically, this extended current layer leads to the formation of a secondary island, breaking the diffusion region into two shorter segments. After the island is ejected, the length of the diffusion region again increases with time until the formation of a new island and the cycle is repeated. In large systems, it appears the ultimate length of the electron diffusion region is limited by the stability of the elongated electron layer to secondary island production. These results suggest a radically different mechanism for the essential physics controlling the reconnection rate.

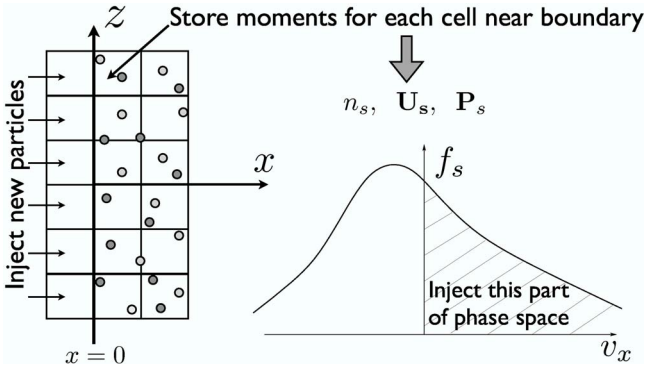

FIG. 2. Particles that reach a boundary are permanently lost, while new particles are injected from the $v_x > 0$ portion of phase space in an attempt to preserve Eq. (1) up through the full pressure tensor.

II. OPEN BOUNDARY MODEL

The new model was developed using an existing parallel PIC code that has been used previously to model current sheet instabilities[43–45] and magnetic reconnection.[27,46] The fields are advanced using a simple explicit algorithm[47,48] while the particles are advanced using the leapfrog technique and moments are accumulated with area weighting. In previous work, periodic boundary conditions were employed for the particles and fields in the outflow direction. Along the transverse boundary, conducting conditions are typically employed for the fields while the particles are reflected.

To improve upon these simple boundary conditions, a range of difficult issues are introduced. In particular, the question of precisely what conditions constitute a physically meaningful boundary value problem has not been rigorously solved even for ideal MHD.[49] A perfect open system would permit all the characteristics to cross the boundary smoothly. Due to the long list of possible waves in the Vlasov-Maxwell description, it is not clear how to accomplish this in general. For the purpose of this work, the focus has been have limited to boundary conditions that are open with respect to particles, magnetic flux, and electromagnetic radiation.

A. Particle boundary condition

To model an open boundary, a zero normal derivative condition is often applied to the fluid moments in MHD,[21,49] Hall MHD,[16,33] and hybrid[34] simulations of magnetic reconnection. While this type of boundary condition is conceptually simple, it is difficult to implement in a PIC code since the calculation involves the time evolution of Lagrangian tracer particles. To enforce a boundary condition on the moments, one must instead specify how particles enter and leave the system. Due to the particle discreteness, any such boundary condition on the moments is only approximately satisfied during any given time interval. In large-scale hybrid simulations of reconnection,[34] this type of condition was applied in an approximate manner for the first two moments of the ion distribution.

Motivated by this previous work, we propose a new technique for applying the zero normal derivative condition to the moments up through all elements of the pressure tensor for each species. The basic idea for the particle boundary condition is illustrated in Fig. 2. When a particle crosses a boundary in the outward direction it is permanently lost, but new particles are injected at each time step in an attempt to maintain a zero normal derivative condition on the first three moments

$$\frac{\partial \langle f_s v_m^i v_k^j \rangle}{\partial \mathbf{n}} = 0, \tag{1}$$

where f_s is the distribution function of species s, $\langle\ \rangle$ represents velocity space integration, $i+j \leqslant 2$ to treat moments up through the pressure tensor, $\mathbf{n}$ is the normal direction for the boundary in question, and $m,k=x,y,z$ signify the components of the velocity. Aside from the issue of a scalar versus a tensor pressure, this boundary condition is consistent with previous fluid simulations.[16,21] However, it is not possible to apply this condition precisely at any given instant due to the inherent statistical fluctuations in PIC simulation. In fluid simulations, rigorously enforcing a zero normal derivative on the moments is known to produce reflection of waves.[49] In contrast for a PIC simulation, the information is carried by the particles which are free to leave the system without difficulty. Thus when a longitudinal wave interacts with the boundary, the particle correlations are destroyed which tends to minimize reflections.

The more difficult problem is to specify the inward flux of particles from the plasma that would exist just outside the simulation domain for a larger system. The boundary condition in Eq. (1) implies that the moments just outside the system are equal to the moments near the boundary. Thus to approximately enforce Eq. (1), we assume that the distribution function in the region near the boundary may be approximately characterized by a quadratic form

$$f_s = C_s \exp[-(\mathbf{v} - \mathbf{U}_s) \cdot \mathbf{W}_s \cdot (\mathbf{v} - \mathbf{U}_s)], \tag{2}$$

where C_s is a normalization constant, $\mathbf{U}_s$ is the fluid velocity, and $\mathbf{W}_s$ is an unknown tensor. These constants are determined for each ghost cell by the first three moments of the distributions

$$n_s = \int f_s d^3\mathbf{v},$$

$$\mathbf{U}_s = \int \mathbf{v} f_s d^3\mathbf{v}, \tag{3}$$

$$\mathbf{P}_s = m_s \int (\mathbf{v}-\mathbf{U}_s)(\mathbf{v}-\mathbf{U}_s) f_s d^3\mathbf{v},$$

in the boundary region immediately inside the simulation. Performing the integration results in

$$C_s = \frac{n_s\sqrt{\det(\mathbf{W}_s)}}{\pi^{3/2}}, \quad \mathbf{W}_s = \frac{m_s n_s}{2}\mathbf{P}_s^{-1}, \tag{4}$$

so that by computing the inverse of the pressure tensor $\mathbf{P}_s^{-1}$ the quadratic form for the corresponding distribution is immediately obtained. The flexibility of allowing a full pressure tensor is important for kinetic simulations of reconnection for a number of reasons. Even if the distributions are gyrotropic, in the presence of temperature anisotropy ($T_{\parallel_s} \neq T_{\perp_s}$) the pressure tensor is not diagonal in the simulation frame (although it is diagonal in the local magnetic frame). In addition, previous periodic simulations of reconnection indicate both temperature anisotropy as well as some degree of agyrotropy at the outflow boundaries. The assumed distribution in Eq. (2) permits both of these possibilities yet only requires the moments in the simulation frame (i.e., not necessary to transform $\mathbf{P}_s$ to local magnetic frame).

The distribution function for each ghost cell surrounding the domain is characterized by Eq. (2) where the moments are determined by the measured values in the interior cells immediately adjacent. Due to the statistical noise in a PIC simulation, it is necessary to average the computed moments. To reduce the short scale spatial fluctuations, a standard 9-point spatial filter[50] is employed. In addition, the calculated moments are time averaged using a simple relaxation scheme

$$M_s^{\text{new}} = RM_s + (1-R)M_s^{\text{old}}, \tag{5}$$

where M_s^{new} is the new moment, M_s is the computed moment immediately inside the domain at a given time step, M_s^{old} is the old value of the moment, and $0 < R \leqslant 1$ is a relaxation coefficient that controls how rapidly the moments in the ghost cell are permitted to change. The spatial and temporal smoothing is applied to the moments for each species ($M_s = n_s, \mathbf{U}_s, \mathbf{P}_s$), and the coefficient R is selected to average on the Ω_{ci} time scale.

The only remaining problem is to properly sample the distribution in Eq. (2) in order to inject the correct number of particles with appropriate inward velocities at each time step in the calculation. Although the same particle boundary condition is applied on all boundaries, for notational simplicity consider the boundary shown in Fig. 2 with normal in the x direction. At a position z along this boundary, the inward flux of particles with normal velocity less than v_x is

$$\Gamma_s(z,v_x,t) = \int_{-\infty}^{\infty}\int_{-\infty}^{\infty}\int_{0}^{v_x} v_x' f_s(z,\mathbf{v}',t) dv_x' dv_y' dv_z', \tag{6}$$

while the total inward flux is $\Gamma_{so}(z,t) \equiv \Gamma_s(z,\infty,t)$. For the assumed form of the distribution in Eq. (2), the integrals simplify to

$$\Gamma_s = \frac{n_s V_{sx}}{2\pi^{1/2}}\left\{\exp\left(-\frac{U_x^2}{V_{sx}^2}\right) - \exp\left(-\frac{(v_x-U_x)^2}{V_{sx}^2}\right) + \pi^{1/2}\frac{U_x}{V_{sx}}\left[\operatorname{erf}\left(\frac{v_x-U_x}{V_{sx}}\right) + \operatorname{erf}\left(\frac{U_x}{V_{sx}}\right)\right]\right\}, \tag{7}$$

where $V_{sx}^2 \equiv 2P_{xx}/(m_s n_s)$ and Γ_s, U_x, and V_{sx} are functions of z and t [continuously updated with Eq. (5)]. To compute the number of particles to inject, the total inward flux is integrated across the cell size in the transverse direction and then integrated as a function of time

$$N_j = \Delta_z \int_0^t \Gamma_{so}(z_j,t')dt', \tag{8}$$

where N_j is the total number of particles injected from the ghost cell centered at z_j and Δ_z is the transverse width of the cell. This expression is continually updated with N_j stored as a real number. However, only an integer number of particles are injected at each time step with the remainder accumulated for future injections.

For a given ghost cell, the probability that a particle with normal velocity less than or equal to v_x (but any possible transverse velocity) will cross into the system is proportional to $\Gamma_s(z_j,v_x,t)$. To sample the distribution, one must normalize by the total inward flux

$$\frac{\Gamma_s(z_j,v_x,t)}{\Gamma_{so}(z_j,t)} = R_x, \tag{9}$$

where R_x is a uniform random deviate between [0,1]. Using Γ_s in Eq. (7), this equation is solved numerically to compute v_x for each R_x. Next, the transverse velocity components must be chosen in a manner consistent with the assumed distribution. Assuming v_x is known from the solution of Eq. (9), the probability that the particle will have a velocity less than or equal to v_y (but with any possible v_z) is

$$\frac{\int_{-\infty}^{\infty}\int_{-\infty}^{v_y} f_s(z_j,v_x,v_y',v_z')dv_y'dv_z'}{\int_{-\infty}^{\infty}\int_{-\infty}^{\infty} f_s(z_j,v_x,v_y',v_z')dv_y'dv_z'} = R_y, \tag{10}$$

where R_y is a uniform random deviate between [0,1]. Performing the integration and solving for v_y results in

$$v_y = U_y + \operatorname{erf}^{-1}(2R_y-1)\left(\frac{W_{zz}}{W_{yy}W_{zz}-W_{yz}^2}\right)^{1/2} + (v_x-U_x)\frac{P_{xy}}{P_{xx}}. \tag{11}$$

With both v_x and v_y known, the v_z component is calculated from the ratio

$$\frac{\int_{-\infty}^{v_z} f(z_j, v_x, v_y, v_z')dv_z'}{\int_{-\infty}^{\infty} f(z_j, v_x, v_y, v_z')dv_z'} = R_z, \tag{12}$$

where R_z is a uniform random deviate. Performing the integration and solving for v_z results in

$$v_z = U_z + \frac{1}{W_{zz}}[\sqrt{W_{zz}}\,\mathrm{erf}^{-1}(2R_z - 1) - (v_x - U_x)W_{xz} - (v_y - U_y)W_{yz}]. \tag{13}$$

To summarize, the number of particles to inject inward for each ghost cell is computed by the time integration of the inward flux as shown in Eq. (8). To properly sample the distribution, the velocity for each injected particle is chosen based on three random numbers and Eqs. (9), (11), and (13). This method assures that the reinjected particles are completely uncorrelated with those leaving the box, but are statistically sampled from a distribution possessing the same time-averaged moments.

B. Field boundary condition

In the PIC code employed for this research, the fields are advanced using the scalar and vector potentials

$$\mathbf{B} = \nabla \times \mathbf{A},$$

$$\mathbf{E} = -\nabla\phi - \frac{1}{c}\frac{\partial \mathbf{A}}{\partial t}.$$

In the Coulomb gauge $\nabla \cdot \mathbf{A} = 0$, Maxwell's equations take the form

$$\nabla^2 \mathbf{A} - \frac{1}{c^2}\frac{\partial^2 \mathbf{A}}{\partial t^2} = -\frac{4\pi}{c}\mathbf{J} + \frac{1}{c}\frac{\partial \nabla \phi}{\partial t}, \tag{14}$$

$$\nabla^2 \phi = -4\pi\rho. \tag{15}$$

These equations are solved using a standard explicit approach.[47,48,50] Since area weighting is used to interpolate the particle information to the grid, the resulting ρ and $\mathbf{J}$ do not satisfy the continuity equation to numerical round-off. To correct for this small inconsistency, the auxiliary equation

$$\nabla^2 \frac{\partial \phi}{\partial t} = 4\pi \nabla \cdot \mathbf{J}, \tag{16}$$

is used to compute the electrostatic contribution to the displacement current $\partial\phi/\partial t$ in Eq. (14). This approach guarantees that the gauge condition is preserved to numerical round-off at each time step.[47,48]

Boundary conditions are required for each component of $\mathbf{A}$ as well as ϕ around the perimeter of the system. It is difficult to physically justify the proper form for the electrostatic boundary condition along an open boundary. Nevertheless, due to the strong nature of Debye screening in plasmas, there is some hope that the results may be fairly insensitive to the precise condition, provided the existence of some essential feature is not precluded. In particular, previous simulations indicate strong electrostatic field structures extending outward along the separatrices. Enforcing a $\phi = 0$ condition around the entire perimeter would not allow such a structure to extend smoothly to the outflow boundary. To relax this condition, one may introduce a vacuum gap and move the spatial location of where $\phi = 0$ is applied to some distance Δ_v outside the system as shown in Fig. 3. The gap distance Δ_v may be either finite or infinite using a standard technique.[36,50] For this manuscript, the gap was chosen to be 5% of the box length in the outflow direction, but the essential results (i.e., reconnection rate) are highly insensitive to the precise value of Δ_v. The electrostatic boundary conditions shown in Fig. 3 are employed for both Eq. (15) and Eq. (16).

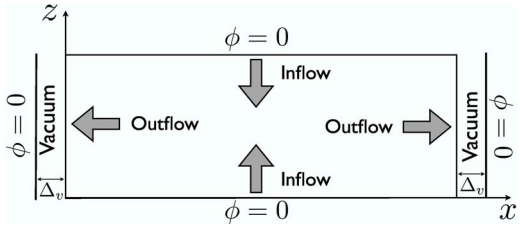

FIG. 3. Electrostatic boundary condition employed for Eqs. (15) and (16). In the outflow direction, a vacuum gap is introduced so that the $\phi = 0$ condition is applied at some distance Δ_v outside the system.

In choosing the boundary conditions for the vector potential, we are guided by previous MHD (Ref. 21) and Hall MHD (Ref. 16) simulations in which the normal derivative of the transverse components of $\mathbf{B}$ are set to zero at the boundary. Unfortunately, the direct implementation of this condition results in the steady accumulation of short wavelength electromagnetic noise that eventually overwhelms the reconnection electric field. Fortunately, it is possible to modify the boundary conditions to permit radiation to leave the system while approximately retaining the same long time behavior. In this regard, the most important boundary condition is for the out-of-plane vector potential A_y, since this determines the in-plane magnetic field. To justify this boundary condition, consider the normal derivative of the y component of Eq. (14) at the outflow boundary

$$\nabla^2 \frac{\partial A_y}{\partial x} - \frac{1}{c^2}\frac{\partial^2}{\partial t^2}\frac{\partial A_y}{\partial x} = -\frac{4\pi}{c}\frac{\partial J_y}{\partial x} = 0,$$

where the last equality is due to the particle boundary condition in Eq. (1). Now assuming the dominant contribution to the Laplacian operator at the boundary is $\nabla^2 \approx \partial^2/\partial x^2$, this equation may be factored

$$\left(\frac{1}{c}\frac{\partial}{\partial t} - \frac{\partial}{\partial x}\right)\left(\frac{1}{c}\frac{\partial}{\partial t} + \frac{\partial}{\partial x}\right)B_z \approx 0, \tag{17}$$

where $B_z = \partial A_y/\partial x$. At the left and right outflow boundaries, the appropriate sign is selected to match the outward propagating solution. The same line of reasoning applies at the inflow boundaries, but the normal derivative is $\partial/\partial z$ and the resulting wave equation is for B_x. These boundary conditions permit electromagnetic radiation (polarized out-of-plane) to leave the system. Averaging over the rapid time scale asso-

Inflow	Outflow	Physics
$\frac{\partial A_x}{\partial t} \pm c\frac{\partial A_x}{\partial z} = 0$	$\frac{\partial A_z}{\partial t} \pm c\frac{\partial A_z}{\partial x} = 0$	Absorb EM waves
$\frac{\partial A_z}{\partial z} = -\frac{\partial A_x}{\partial x}$	$\frac{\partial A_x}{\partial x} = -\frac{\partial A_z}{\partial z}$	Gauge Condition
$\frac{\partial^2 A_y}{\partial t \partial z} \pm c\frac{\partial^2 A_y}{\partial z^2} = 0$	$\frac{\partial^2 A_y}{\partial t \partial x} \pm c\frac{\partial^2 A_y}{\partial x^2} = 0$	Absorb EM waves & set average normal derivative of B to zero

FIG. 4. Summary of electromagnetic boundary conditions. To match the outgoing waves, the positive signs apply to the right and top boundaries while the negative signs apply to the left and bottom boundaries.

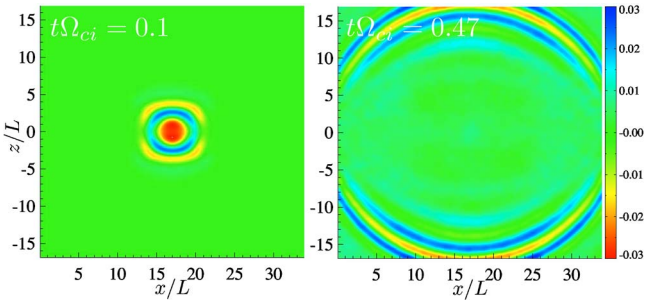

FIG. 5. (Color online) The out-of-plane electric field E_y resulting from a large amplitude perturbation localized in the center of the box at $t=0$. The impulse launches an outward propagating radiation front which is shown at an early time (left) and at a later time (right) to demonstrate that light waves leave the system.

ciated with light waves, these boundary conditions reduce to $\partial B_z/\partial x \approx 0$ along the outflow, while $\partial B_x/\partial z \approx 0$ along the inflow.

For the in-plane components of the vector potential, a standard radiation boundary condition[50,51] is employed, to allow electromagnetic waves with in-plane polarization to leave the system. This boundary condition is commonly used in kinetic simulations of laser-plasma interactions, and also corresponds to matching with an outward propagating plane-wave solution. This condition is implemented on the transverse in-plane component of **A**, while the normal component is constrained by the gauge condition. For waves at normal incidence, these simple boundary conditions give complete absorption while for an incident angle of 45° the reflection is approximately 17% or 3% in terms of energy.[50] There are techniques for improving these simple boundary conditions to obtain nearly complete absorption.[52,53] However, these techniques are significantly more complicated and the simple method appears adequate to avoid the accumulation of radiation previously mentioned.

The electromagnetic boundary conditions employed for each component of **A** are summarized in Fig. 4. Notice these conditions are symmetric with respect to the inflow and outflow boundaries, and are thus appropriate to model an undriven reconnection.

C. Test of particle injectors

The new particle injection algorithm was tested separately from the implementation in the PIC code using the following approach. There are ten scalar input quantities to the algorithm (n_s, $\mathbf{U}_s$, and $\mathbf{P}_s$) along with the specification of the boundary normal direction. For the boundary shown in Fig. 2 with normal in the positive x direction, the injection algorithm samples from the $v_x > 0$ region of phase space, while if the normal direction is reversed the algorithm samples from the $v_x < 0$ region. By combining the leftward plus the rightward injections, the entire distribution is sampled and one may directly reconstruct the moments from the particle velocities obtained from the algorithm. This procedure accurately reproduces the desired input moments indicating the method is conceptually correct and properly implemented.

D. Test of radiation boundary condition

To demonstrate that the boundary conditions are open with respect to electromagnetic radiation, a number of Harris sheet simulations were initialized with a large amplitude perturbation δA_y, highly localized in the center of the box. This sudden impulse launches a large amplitude radiation front that propagates outward at the velocity of light. An example is shown in Fig. 5 at an early time shortly after the impulse is generated and at a later time as the waves leave the system. By closely examining a number of such simulations, it is clear that reflections at the boundaries are quite minimal and over longer periods of time there is no observable accumulation of electromagnetic radiation in the system. The interaction of other types of waves with the boundary has not been systematically studied. However, it is expected that any wave with a longitudinal component will be damped to some degree, since particle correlations are destroyed by the particle boundary condition.

E. Description of diagnostics employed

Energy conservation: As a standard consistency check, the energy conservation equation for the fields is evaluated in integral form

$$\frac{d}{dt}\int\left(\frac{B^2}{8\pi}+\frac{E^2}{8\pi}\right)dV+\int \mathbf{S}\cdot d\mathbf{a}+\int \mathbf{E}\cdot\mathbf{J}dV=0,$$

where $\mathbf{S}=c(\mathbf{E}\times\mathbf{B})/4\pi$ is the Poynting flux. The flow of electromagnetic energy into and out of the simulation domain is evaluated by computing $\mathbf{S}\cdot d\mathbf{a}$ along each boundary. The total field energy and the energy exchanged with the particles ($\mathbf{E}\cdot\mathbf{J}$) are both integrated over the domain at each time step. Typical open boundary calculations satisfy this equation to an accuracy of about 1% over 2×10^5 time steps, which is comparable to the energy conservation with periodic boundary conditions.

Reconnection rate: For 2D steady-state reconnection, the out-of-plane electric field should be a constant across the simulation domain. Thus to evaluate the steadiness of reconnection and measure the reconnection rate, the out-of-plane electric field is evaluated at three locations: (1) in the center of the box (i.e., near the x-point), (2) at the center of the two inflow boundaries, and (3) at the center of the two outflow

boundaries. Steady-state reconnection is achieved only when these three electric field measurements approximately balance over some time interval. Since the instantaneous electric fields are noisy, the normalized reconnection rate is computed from

$$E_R \equiv \frac{1}{B_o V_A}\left\langle \frac{\partial A_y}{\partial t} \right\rangle, \tag{18}$$

where $\langle\ \rangle$ denotes the average over a time interval $4\Omega_{ci}^{-1}$, and $V_A = B_o/\sqrt{4\pi n_b m_i}$ is the Alfvén velocity based on the initial magnetic field B_o and density n_b at the inflow boundary.

Streamlines: The streamlines for the ion and electron flow velocities are useful to quickly visualize the structure of the layer. However, the stream function is only rigorously defined for incompressible flow $\nabla \cdot \mathbf{U}_s = 0$, while PIC simulations are compressible. Nevertheless, compressibility effects are fairly small in most regions and one may still define an approximate stream function $\mathbf{U_s} = \nabla \times \boldsymbol{\Psi}$. For 2D simulations, the out-of-plane component of the stream function is then computed from $\nabla^2 \Psi_y = -(\nabla \times \mathbf{U}_s)_y$. The consistency of this approach is checked afterwards by evaluating $\mathbf{U_s} \cdot \nabla \Psi_y = |U_s||\nabla \Psi_y| \cos(\theta)$ with typical results $\theta \approx 85° \rightarrow 90°$ indicating the approximate streamlines are sufficiently accurate for the purpose of visualization.

III. RECONNECTION IN A NEUTRAL SHEET

All simulations discussed in this manuscript employ a Harris sheet[54] for the initial configuration with magnetic field $B_x = B_o \tanh(z/L)$, where L is the half-thickness of the layer. The density profile for the Harris distribution is $n = n_o \operatorname{sech}^2(z/L)$ and the distribution functions for each species are initialized as drifting Maxwellians. In addition, a uniform background plasma is introduced with density n_b, zero net drift and the same temperature as the Harris distributions. Although the background plasma does not modify the force balance, it is essential to include so that new plasma can flow into the diffusion region and so that the distribution is well characterized along all boundaries. The time averaging in Eq. (5) requires an initial distribution for each ghost cell which is specified by the initial distribution immediately inside the simulation domain. For this manuscript, the initial simulation parameters are

$$\frac{\rho_i}{L} = 1, \quad \frac{m_i}{m_e} = 25, \quad \frac{T_i}{T_e} = 5, \quad \frac{\omega_{pe}}{\Omega_{ce}} = 3, \quad \frac{n_b}{n_o} = 0.3, \tag{19}$$

where $\rho_i = v_{\mathrm{th}_i}/\Omega_{ci}$ is an ion gyroradius, $v_{\mathrm{th}_i} = (2T_i/m_i)^{1/2}$ is the ion thermal speed, $\Omega_{cs} = eB_o/(m_s c)$ is the gyrofrequency and $\omega_{pe} = (4\pi n_o e^2/m_e)^{1/2}$ is the electron plasma frequency. These parameters imply an electron thermal speed $v_{\mathrm{th}_e} = (2T_e/m_e)^{1/2} \approx 0.136c$. The spatial scales are normalized to the ion inertial length $d_i = c/\omega_{pi}$ where $\omega_{pi} = (4\pi n_o e^2/m_i)^{1/2}$. Time is normalized by the ion gyrofrequency $\Omega_{ci} = eB_o/(m_i c)$ and the fluid velocities for each species are normalized by v_{th_s}.

To initiate reconnection in the center of the simulation domain, a small perturbation is imposed on the out-of-plane vector potential

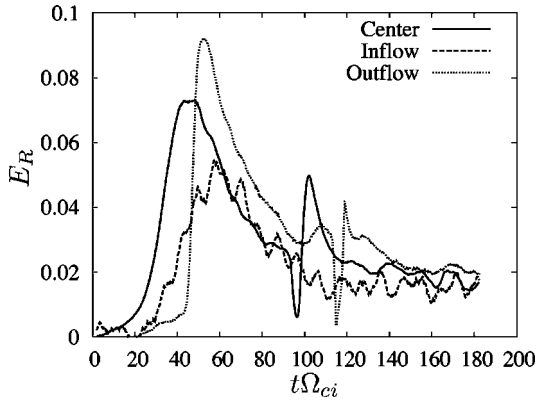

FIG. 6. Reconnection electric field from $25d_i \times 25d_i$ open boundary simulation with parameters given in Eq. (19). The electric field is computed at three locations: (1) at the center of the domain near the x-point, (2) at the center of the inflow boundaries, and (3) at the center of the outflow boundaries.

$$\delta A_y = -A_o \cos\left(\frac{2\pi x}{L_x}\right)\cos\left(\frac{\pi z}{L_z}\right), \tag{20}$$

where L_x and L_z are the box size and $A_o = 0.1 B_o c/\omega_{pi}$.

A. Small open boundary simulation

For the first test case with open boundaries, we consider a relatively small box size $25d_i \times 25d_i$ corresponding to 768×768 cells and 3.75×10^8 computational particles. The time step is $\Delta t \Omega_{ce} = 0.036$ and the simulation is initialized with the small perturbation in Eq. (20) to initiate reconnection in the center of the box. The results in Fig. 6 indicate a peak reconnection rate at the x-point of $E_R \approx 0.073$ near time $t\Omega_{ci} = 45$, followed by a slow decrease until an approximate steady-state value $E_R \approx 0.018$ is achieved for $t\Omega_{ci} > 135$.

Although the maximum reconnection rate at the x-point in Fig. 6 is consistent with previous periodic PIC simulations, the subsequent decline and slower steady-state value are quite different. In order to make meaningful comparisons with results in the literature, it is important to normalize the reconnection rate based on conditions just upstream of the ion diffusion region.[15] To convert the results in Fig. 6 to this normalization, it is necessary to examine the plasma density and magnetic field along a vertical slice through the diffusion region. As shown in Fig. 7, changes in the density in the upstream region are relatively small with $n_e/n_b \approx 0.9$ over the time interval $(t\Omega_{ci} = 90 \rightarrow 180)$. Changes in the magnetic field are more significant and depend on the criteria used to identify the upstream edge of the ion diffusion region. Defining the upstream edge by the location where the ion and electron inflows begin to diverge gives approximately $z/d_i \approx 3$ and the magnetic field is $B_x/B_o = 0.83, 0.78, 0.72, 0.71$ for the four times shown. The reconnection rate based on these upstream conditions is $E_R^* = E_R (n_e/n_b)^{1/2} (B_o/B_x)^2$. While this renormalization is important for making comparisons, it does not change the basic shape of the curve in Fig. 6. Using this standard normalization, the peak reconnection rate $E_R^* \approx 0.1$ is in good agreement with previous predictions,[12,16] but the quasisteady rate $E_R^* \approx 0.033$ is signifi-

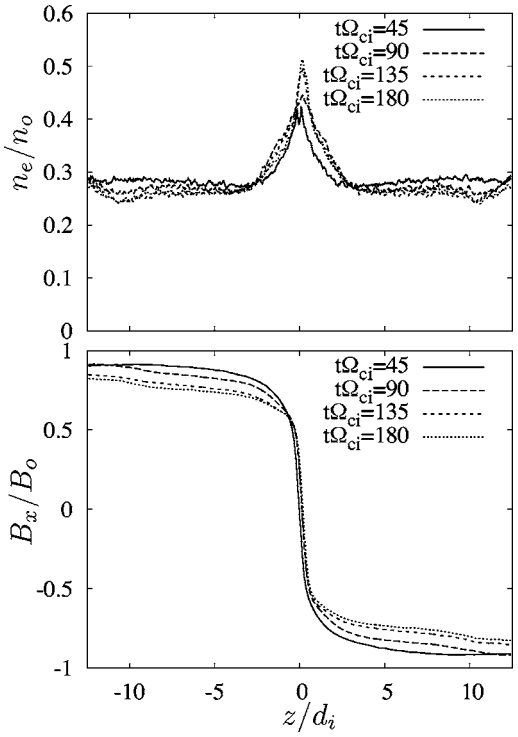

FIG. 7. Density (top) and magnetic field (bottom) along a vertical slice through the diffusion region ($x=12.5d_i$) at four simulation times. At the upstream edge of the ion diffusion region $z/d_i \approx 3$ the magnetic field is $B_x/B_o=0.83,\ 0.78,\ 0.72,\ 0.71$ for the four times shown.

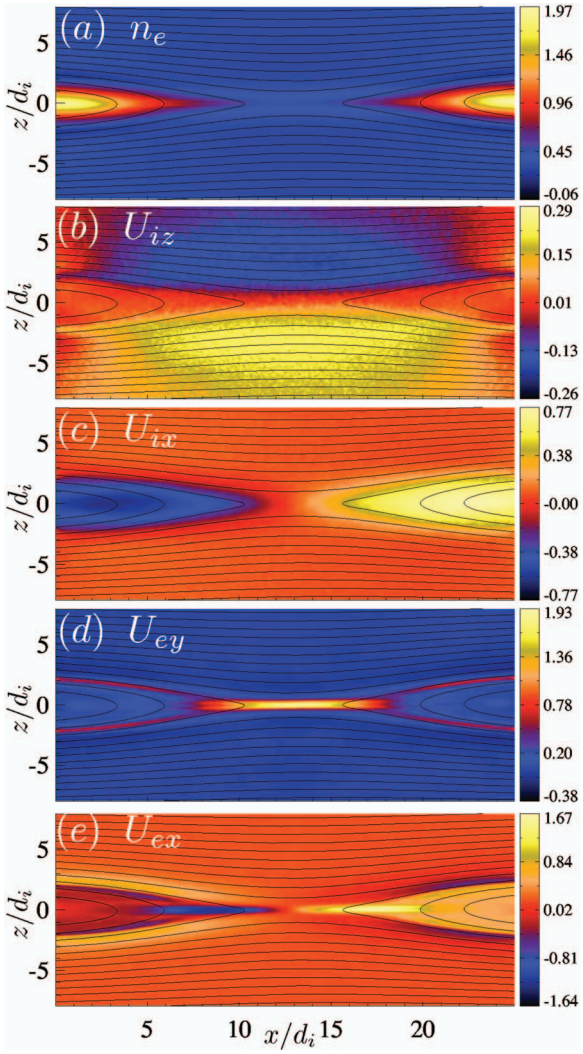

FIG. 8. (Color) Open boundary simulation results for the $25d_i \times 25d_i$ case at time $t\Omega_{ci}=45$ showing contours of (a) electron density n_e, (b) ion inflow velocity U_{iz}, (c) ion outflow velocity U_{ix}, (d) electron out-of-plane velocity U_{ey}, and (e) electron outflow velocity U_{ex}. The black lines denote the flux surfaces, density is normalized by n_o and the velocities are normalized by v_{th_s}.

cantly weaker. It is important to emphasize that this quasi-steady value is achieved over a fairly long time interval $t\Omega_{ci}=135 \rightarrow 180$ and that the corresponding density and magnetic field profiles in Fig. 7 are nearly constant over this interval.

To explore these results in more detail, the basic structure of the reconnection layer is shown in Fig. 8 for a simulation time $t\Omega_{ci}=45$ near the maximum reconnection rate. In the diffusion region of Fig. 8(a), an electron scale structure is visible in the electron density (see also Fig. 7) with depletion regions extending outward along the separatrices. The maximum ion inflow in Fig. 8(b) is $U_{iz}/V_A \approx 0.076$ which is in good agreement with the reconnection rate in Fig. 6 for this time. All moments and fields are well behaved at the outflow boundary, and both plasma and magnetic flux smoothly exit the system as is evident in the ion outflow velocity in Fig. 8(c). Intense electron flows are observed along the separatrices with a structure similar to previous periodic simulations. However, the open boundary conditions eliminate the artificial recirculation and allow the structures along the separatrices to extend smoothly to the outflow boundary as shown in Figs. 8(d) and 8(e).

Although the initial evolution of this open system is consistent with previous periodic simulations, the evolution over longer time scales is markedly different. The standard model of Hall mediated reconnection requires the length of the electron diffusion region to remain microscopic $D_e \lesssim d_i$. In contrast, the electron outflow jets in Fig. 8(e) extend over a significant fraction of the box size. In addition, the current density in the diffusion region forms an extended sheet dominated by the electron out-of-plane velocity shown in Fig. 8(d). As the simulation proceeds past the maximum reconnection rate, the spatial extent of the electron outflow jets steadily increase during the time periodic $t\Omega_{ci}=45 \rightarrow 135$ until the electron diffusion region reaches the simulation boundary. During this stretching process, the reconnected flux is rapidly ejected in the outflow direction by the electron jets and the length of the electron current sheet also increases with time as shown in Fig. 9. Near simulation time $t\Omega_{ci}=95$ the out-of-plane current sheet becomes unstable resulting in the formation of a secondary island. For a brief period, this results in two separate diffusion regions [see Fig. 9(b)] each undergoing fast reconnection. However, the secondary island is ejected from the system before it grows to large amplitude [see Fig. 9(c)], and the electron current sheet again continues to stretch until limited by the box size. The formation of this secondary island and subsequent ejection

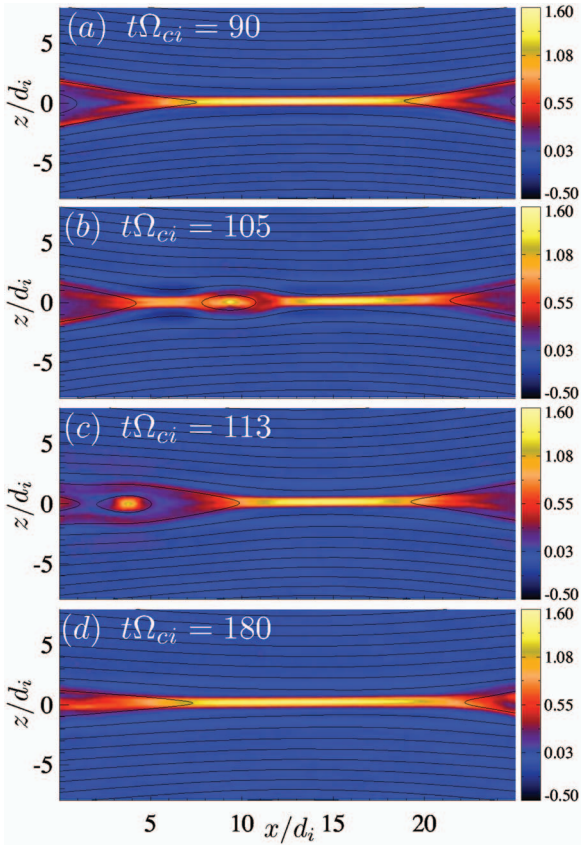

FIG. 9. (Color) Out-of-plane electron velocity U_{ey} at four different simulation times showing the stretching of the electron diffusion region and production of a secondary island. These results are for the $25d_i \times 25d_i$ open boundary case.

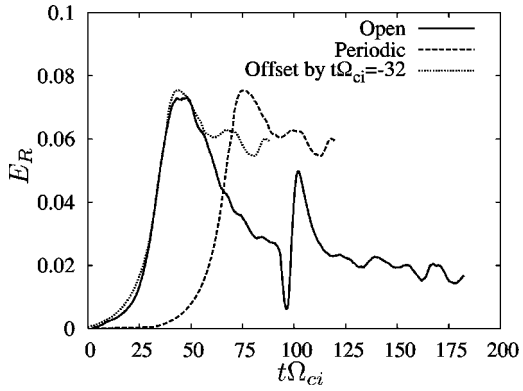

FIG. 10. Comparison of the reconnection electric field in the center of the box (near the x-point) for the $25d_i \times 25d_i$ simulation with open boundary conditions (solid) and $100d_i \times 100d_i$ simulation with periodic boundary conditions (dashed). Since the onset phase is different between these simulations, the periodic results are replotted with a $t\Omega_{ci}=-32$ offset (dotted).

from the system account for the rapid changes visible in the electric field diagnostic in Fig. 6 during the time period $t\Omega_{ci}=90 \rightarrow 120$.

The question of whether this particular case would continue to produce secondary islands is unknown. However, it is not clear that letting this simulation run longer is physically meaningful since the electron diffusion region has stretched all the way to the system boundary. Indeed, the basic motivation for the open boundary model is that gradients (and accelerations) are weak at the boundary. To satisfy this requirement, the domain must be large enough so that the diffusion region is localized away from the boundaries. Based on previous work,[11,12,16] we expected the spatial extent of the electron diffusion region to remain very small $D_e \lesssim d_i$, but instead the length of D_e was limited by the box size in this simulation.

B. Very large periodic simulation

Since these new results are rather surprising, it is important to look for ways to verify the essential predictions while eliminating the influence of the new open boundary conditions. In this regard, one obvious test is to revert back to periodic boundary conditions but with a much larger domain size, and thus allow the simulation to proceed longer before recirculation effects completely dominate. In addition, it is important to increase the flux available for reconnection by increasing the domain size in the inflow direction as well.

For this comparison test, the same equilibrium is used with plasma parameters given in Eq. (19), but the domain size is increased to $100d_i \times 100d_i$. This requires 3072 $\times$ 3072 cells and 5×10^9 computational particles. A standard set of boundary conditions are employed[27,44–46,55] in which both the particles and fields are periodic in the x direction. Along the transverse boundaries, conducting boundary conditions are used for the fields and the particles are reflected. The same initial perturbation in Eq. (20) is used to initiate reconnection.

The reconnection electric field resulting from this large periodic simulation is compared with the much smaller open boundary simulation in Fig. 10. In both cases, the electric field is normalized by the initial upstream conditions as shown in Eq. (18). Although the amplitude A_o of the initial perturbation was the same in both cases, the wavelength in Eq. (20) is set by the box size and is thus four times longer for the periodic case. As a consequence, the onset phase takes longer to develop in the large periodic system as shown in Fig. 10. Nevertheless, after the onset phase the development is remarkably similar.

There are several important points to emphasize in this comparison. After the onset phase, the time development of the reconnection electric field at the x-point is nearly identical up through the maximum reconnection rate. After reaching the same maximum value, both systems indicate a pronounced decrease in the reconnection rate. One pragmatic criterion for judging the open boundary model is its ability to effectively mimic a much larger system. In this regard, it would appear that the open boundary model is quite successful up through $t\Omega_{ci} \approx 55$ where the two curves are nearly identical.

The open and periodic simulation cannot agree indefinitely, since strong recirculation effects eventually dominate the periodic case. The important question is whether the decline in the reconnection rate for the periodic case is due to the stagnation of the reconnection jets or due to stretching of the diffusion region. To examine this question, the ion and

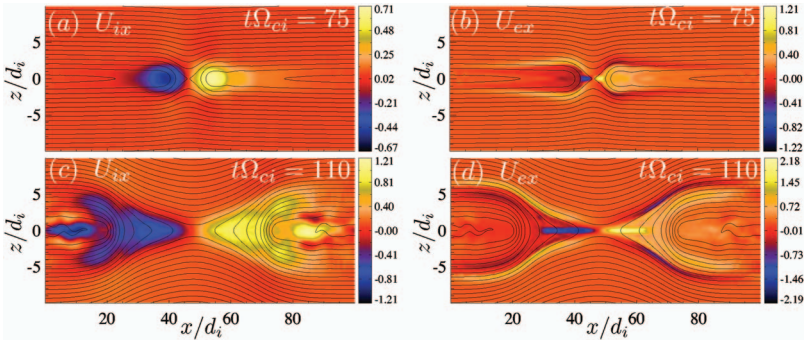

FIG. 11. (Color) Ion outflow velocity U_{ix} (left) and electron outflow velocity U_{ex} (right) for $100d_i \times 100d_i$ simulation with periodic boundary conditions. Results are shown at $t\Omega_{ci}=75$ (top) and $t\Omega_{ci}=110$ (bottom) and are normalized to the initial thermal velocity v_{th_s} for each species. The black lines denote flux surfaces.

electron outflow velocities from the periodic simulation are shown in Fig. 11. At simulation time $t\Omega_{ci}=75$ near the maximum reconnection rate in Fig. 10, the ion outflow jets in Fig. 11(a) extends roughly from $x/d_i \approx 30 \rightarrow 65$, so there is a large region available on each side of the x-point for further expansion of the outflow. Thus the reconnection rate in Fig. 10 begins to decrease long before the jets collide. Strong recirculation is not apparent until much later as shown in Fig. 11(c), where the countersteaming ion jets interpenetrate in the regions $0<x/d_i<20$ and $80<x/d_i<100$.

In the inflow direction, only one tenth of the domain is shown in Fig. 11. Thus the transverse boundary is far removed and does not appear to play any significant role over this time interval. Instead, the reduction in the reconnection rate over the time period $t\Omega_{ci}=75-110$ appears to be the result of stretching of the electron diffusion region. Near the maximum reconnection rate, the spatial scale of the electron outflow jets in Fig. 11(b) is roughly $\pm 3d_i$, but the length increases with time approaching $\pm 15d_i$ at $t\Omega_{ci}=110$ in Fig. 11(d). An elongated out-of-plane electron current sheet is also observed (not shown) to be consistent with the open boundary results.

This large periodic simulation provides strong confirmation of the basic results from the open boundary model. Stretching of the electron diffusion region appears to be an essential feature of neutral sheet reconnection and is not an artifact of the open boundary conditions. Although the rate of stretching is somewhat slower in the periodic simulation, this is to be expected since even at early times there is a small back pressure due to the recirculation of particles and waves. With the open boundary model, this unphysical back pressure is removed and the outward convection of reconnected flux is allowed to proceed in way that is much more realistic.

C. Large open boundary simulation

For the $25d_i \times 25d_i$ open boundary case, the stretching of the electron diffusion region was limited by the box size as shown in Fig. 9. At this point, the electron outflow jets extend to the outflow boundary and the validity of the open boundary model is questionable. To examine the dynamics over longer time scales, it is necessary to increase the size of the domain. In this section, an open boundary simulation is considered with domain size $50d_i \times 50d_i$ corresponding to 1536×1536 cells and requiring 1.5×10^9 computational particles. The same initial equilibrium is employed with parameters in Eq. (19).

The basic structure of the reconnection layer is shown at selected simulation times in Fig. 12. The color contours indicate the out-of-plane electron velocity U_{ey} while the white lines correspond to ion streamlines and black lines are flux surfaces. Throughout the duration of the simulation, pronounced stretching of the electron diffusion region is followed by secondary island production. The first secondary island is visible at time $t\Omega_{ci}=75$ followed by another at $t\Omega_{ci}=110$ (not shown). After each island is produced, the diffusion region is broken into two shorter segments with fast reconnection at each x-point. The flux within the secondary island grows with time until the island is expelled by the

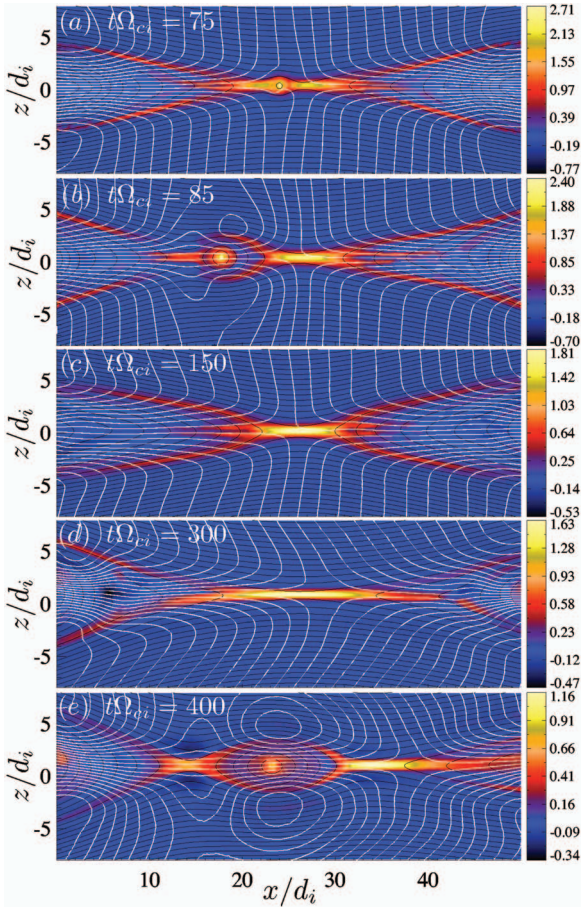

FIG. 12. (Color) Structure of the reconnection layer for the $50d_i \times 50d_i$ open boundary simulation at five selected time slices. Color bar indicates the out-of-plane electron velocity U_{ey} normalized to v_{th_e}. White lines correspond to the ion streamlines and black lines are the flux surfaces.

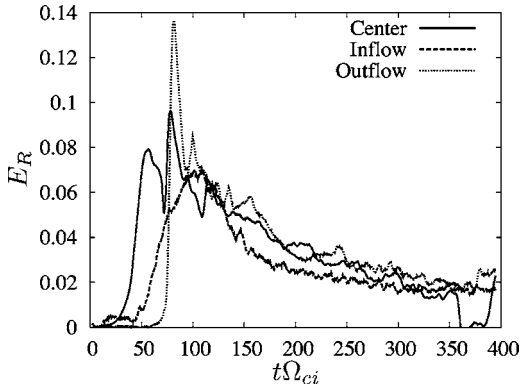

FIG. 13. Reconnection electric field from the $50d_i \times 50d_i$ open boundary simulation with parameters given in Eq. (19). The electric field is computed at three locations: (1) at the center of the domain near the x-point, (2) at the center of the inflow boundaries, and (3) at the center of the outflow boundaries.

electron jets, resulting in a single diffusion region that again stretches with time. After the first two islands are ejected, the diffusion region slowly expands with time as the system relaxes. However, near $t\Omega_{ci} \approx 365$, yet another secondary island is observed to form in the center of the elongated electron current layer. The amplitude of a secondary island is determined by the length of time it is trapped in the system and some islands grow to much larger amplitude as shown in Fig. 12(e) at $t\Omega_{ci} \approx 400$. In contrast to the $25d_i \times 25d_i$ case in Fig. 9, the electron diffusion region does not stretch to the box size for this larger system. Instead, it appears that the length of the electron diffusion region is limited by the productions of secondary islands.

The reconnection electric field for this case is shown in Fig. 13 in the center of the simulation domain and at the center of the inflow and outflow boundaries. The magnitude of the first peak at $t\Omega_{ci} \approx 50$ is in good agreement with the smaller simulation in Fig. 10. Since stretching of the diffusion region is followed by secondary island formation, a true steady state does not exist. Nevertheless, it is interesting to note that the reconnection rate at $t\Omega_{ci} \approx 350$ when the electric field is nearly constant across the system is nearly equal to the quasisteady value in Fig. 6 for the smaller system. Furthermore, the profile of the magnetic field through the diffusion region at this time is in good agreement with the magnetic field profile in Fig. 7 at $t\Omega_{ci} = 180$ for the smaller system, while the corresponding density profile is approximately 12% lower in the larger system. Thus to renormalize the rates in Fig. 13 based on the density and magnetic field upstream of the ion diffusion region, the numerical factors are essentially the same as already discussed in Fig. 6 for the smaller system. The time scale for the three electric field measurements to approximately balance is about a factor of 2 longer in Fig. 13 than for smaller system in Fig. 6.

IV. INTERPRETATION OF RESULTS

Since the new results in this manuscript pose a serious challenge to the standard model of Hall mediated reconnection,[9–15] it is important to review the reasoning that led to this model. The diffusion region for each species (see Fig. 1) is usually defined by the spatial region in which the frozen-in condition is violated $\mathbf{E}+\mathbf{U}_s \times \mathbf{B} \neq 0$. It is typically argued that the thickness of the ion diffusion region is of order $\delta_i \sim d_i$ while the width of the electron diffusion region is of order $\delta_e \sim d_e$. A Sweet-Parker-type analysis is applied to each diffusion region, starting with the inner electron region. Due to the Hall dynamics, the electron outflow velocity is limited by the phase speed of a whistler wave $\omega/k \approx k d_e V_{Ae}$ where $V_{Ae} = B/\sqrt{4\pi n m_e}$ is the electron Alfvén speed based on conditions just upstream of the electron diffusion region. Assuming incompressibility, mass conservation implies $\delta_e U^e_{\text{out}} = D_e U^e_{\text{in}}$, where δ_e is the width and D_e is the length of the electron diffusion region. Choosing the wave vector $k \sim 1/\delta_e$ results in

$$U^e_{\text{in}} \sim \frac{d_e}{D_e} V_{Ae}. \tag{21}$$

Thus it is argued that the dispersive properties of the whistler wave results in a reconnection rate that is independent of δ_e and therefore the mechanism that breaks the frozen-in condition. Clearly for this argument to hold, D_e must also be independent of the mechanism that breaks the frozen-in condition. Previous results from kinetic[11] and two-fluid[12] simulations predicted the electron diffusion region remains microscopic in both directions with $D_e \lesssim d_i$. Assuming this is correct, the maximum rate permitted by the electrons in Eq. (21) is very large and there is no electron "bottleneck." The actual reconnection rate is then determined by the ions in the outer region, and the electrons slow down to adjust.

A Sweet-Parker analysis applied to the outer region implies that the outflow is limited by the ion Alfvén velocity V_{Ai} based on the conditions upstream of the ion diffusion region. Together with mass conservation, this implies $U_{\text{in}}/V_{Ai} \approx d_i/D_i$, so that the length of the ion diffusion region D_i determines the reconnection rate. Using results from large-scale two fluid simulations, it has been argued that whistler physics near the x-line leads to a value of $D_i \approx 10 d_i$ resulting in a "universal" reconnection rate $U_{\text{in}} \approx 0.1 V_{Ai}$ independent of system size and plasma parameters.[12,15] This model is supported by large-scale two-fluid simulations and much smaller kinetic simulations. However, the fluid models contain many approximations while the previous kinetic simulations were limited by periodic boundary conditions and system size.

The new results in this manuscript point to a serious problem with this standard picture. When fully kinetic simulations are allowed to proceed over longer time scales, the length D_e of the electron diffusion region increases far beyond any previous expectation. It is important to emphasize that this result is clearly evident with both open boundary conditions and with large-scale periodic simulations. In each case, the electron outflow approximately satisfies the expectation $U_{ex} \leqslant V_{Ae}$. At early time when D_e is relatively short, the rate in Eq. (21) is large enough so that the electrons do not form a bottleneck and the ions determine the reconnection rate. However, as the length of D_e increases with time, the electrons become the bottleneck and the reconnection rate is no longer independent of the electron physics.

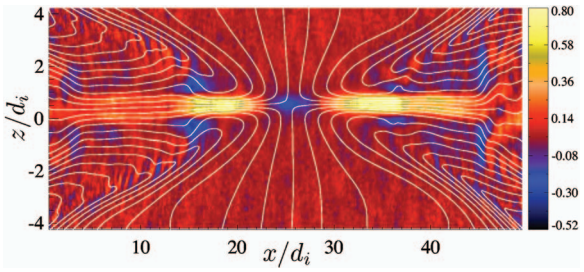

FIG. 14. (Color) Color contours of $(\mathbf{E}+\mathbf{U_e}\times\mathbf{B})_y$ at $t\Omega_{ci}=100$ for the $50d_i \times 50d_i$ open boundary simulation. The white lines are the approximate streamlines for the electron flow.

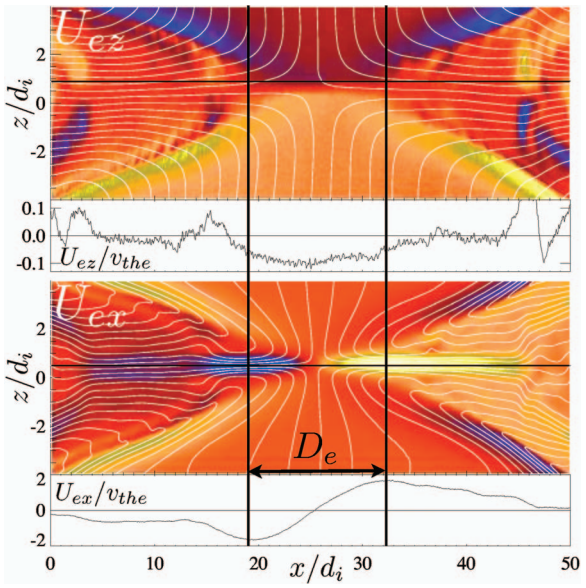

FIG. 15. (Color) Electron inflow velocity U_{ez} (top) and outflow velocity U_{ex} (bottom) for $50d_i \times 50d_i$ open boundary simulation at time $t\Omega_{ci}=100$. The profiles are shown along the horizontal cuts (black lines). In the upper figure, the cut is at $z/d_i=0.9$ corresponding to the upstream edge of electron diffusion region, while in the bottom figure the profile is along the center of the outflow jet $(z/d_i=0.5)$. White lines indicate the approximate electron streamlines. The length of the electron diffusion region D_e is defined by the peak outflow velocity.

To make this argument quantitative, it is necessary to explicitly evaluate the aspect ratio of the electron and ion diffusion regions. Typically, these are defined by the spatial region in which $\mathbf{E}+\mathbf{U}_s\times\mathbf{B}\neq 0$ as illustrated in Fig. 14 for the electrons. Inside this region, the nonideal electric field is balanced by $\nabla\cdot\mathbf{P}_e$ and/or electron inertia.[55] While the relevant width δ_e is fairly well defined by this criteria, the length D_e is more ambiguous since the nonideal region in Fig. 14 extends to the entire length of the electron outflow jet, well beyond the region of significant electron inflow (see electron streamlines in Fig. 14). For the purpose of estimating the reconnection rate based on a Sweet-Parker-type analysis, the proper length for D_e corresponds to the region of nearly uniform inflow as illustrated in Fig. 15. Mass conservation then implies that the electron outflow velocity is a maximum at the downstream edge of the electron diffusion region. Thus we define δ_e based on the full width at half maximum of $\mathbf{E}+\mathbf{U}_e\times\mathbf{B}\neq 0$ while the length D_e is defined by the spatial location of the maximum outflow velocity. For the example shown in Fig. 15, we obtain $\delta_e\approx 3.5d_e$ and $D_e\approx 14d_i$. The width of the ion diffusion region δ_i is defined by the spatial location where the electron and ion inflow velocities begin to diverge while the length D_i is defined by the spatial location of the maximum ion outflow velocity.

Using these aspect ratios, the maximum possible reconnection rate through each diffusion region is estimated by assuming a limiting outflow velocity and then imposing mass conservation. For the inner region, the electron outflow velocity is presumably limited by $U^e_{\rm out}\leqslant V_{Ae}$ resulting in a maximum reconnection rate

$$E_R=\left(\frac{B_{\delta_e}}{B_o}\right)^2\left(\frac{n_b}{n_{\delta_e}}\right)^{1/2}\left(\frac{m_i}{m_e}\right)^{1/2}\frac{\delta_e}{D_e}, \tag{22}$$

where for consistency we have normalized by the ion Alfvén velocity based on B_o and n_b [same as Eq. (18) and all other figures], and B_{δ_e}, n_{δ_e} are the magnetic field and density at the upstream edge of the electron diffusion region. For the outer region, the limiting outflow velocity is $U_{\rm out}\leqslant V_{Ai}$ resulting in a maximum rate

$$E_R=\left(\frac{B_{\delta_i}}{B_o}\right)^2\left(\frac{n_b}{n_{\delta_i}}\right)^{1/2}\frac{\delta_i}{D_i}, \tag{23}$$

where B_{δ_i}, n_{δ_i} are the magnetic field and density at the upstream edge of the ion diffusion region. These expressions are fairly sensitive to the upstream value of the magnetic field and thus the precise value chosen for δ_e and δ_i. To account for this uncertainty, the limiting rates are evaluated over a reasonable range of widths. For the $50d_i\times 50d_i$ open boundary case, we estimate $\delta_e/d_e\approx 3\rightarrow 4$ and $\delta_i/d_i\approx 5\rightarrow 6$ over the duration of the run. The lengths D_i and D_e for this case are shown in the top panel of Fig. 16 as a function of time. Using these lengths, the limiting expressions in Eqs. (22) and (23) are compared against the actual reconnection rate in the bottom panel. The shaded regions correspond to the degree of uncertainty in specifying the width of each diffusion region. The limiting expressions are not really meaningful in the initial phase $t\Omega_{ci}=0-50$ since reconnection is just getting started. During the time interval $t\Omega_{ci}=70-120$, it appears that reconnection is limited by the ions, but it is very difficult to estimate D_e since there are two secondary islands generated during this interval. Furthermore, it is doubtful that a simplified Sweet-Parker analysis can be applied when there are multiple diffusion regions and dynamically evolving islands. However, during the time interval $t\Omega_{ci}=130-350$ there is a single x-point and the actual reconnection rate decreases in good agreement with the electron limit in Eq. (22). In addition, the length of the electron diffusion region in the top panel increases by a factor of ~ 3 over this same interval. These results clearly demonstrate that the electrons are limiting the reconnection rate due to the stretching of the electron diffusion region.

In fully kinetic simulations, the self-consistent evolution of the magnetic field controls the nature of the electron orbits in the various regions of the layer. Thus the profile of B_z in the outflow direction may strongly influence the length D_e

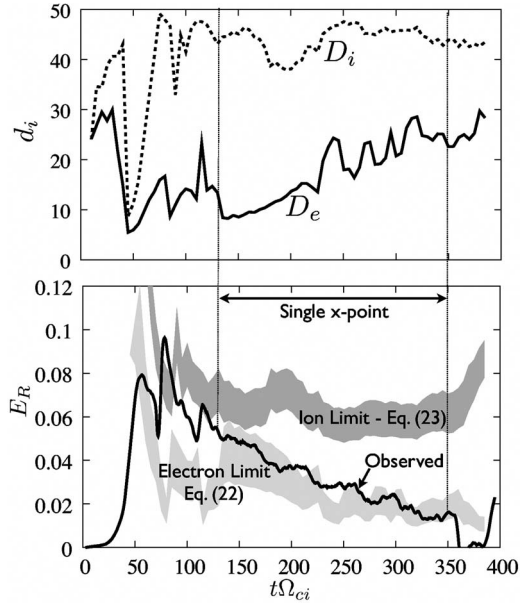

FIG. 16. Length of the ion D_i and electron D_e diffusion regions (top) and estimates for the limiting reconnection rate through each diffusion region (bottom) for the $50d_i \times 50d_i$ open boundary simulation. The solid black line in the bottom figure corresponds to the observed reconnection electric field at the center of the box. The electron limit is evaluated from Eq. (22) with $\delta_e/d_e \approx 3 \rightarrow 4$ while the ion limit is evaluated from Eq. (23) with $\delta_i/d_i \approx 5 \rightarrow 6$.

due to the spatial extent of meandering electron orbits. To properly model the electron diffusion region, it is essential to allow reconnected flux to be transported away from the x-point in some realistic fashion. With periodic boundary conditions, the outflow of reconnected flux is trapped in the system which artificially constrains the size of the diffusion region. Nevertheless, for very large periodic systems the stretching process is clearly evident as demonstrated in Fig. 11(d). Since the reconnected flux is rapidly convected outwards by the electrons jets, to maintain a short diffusion region requires some mechanism to regenerate sufficient B_z field to balance the outward convection. In the context of MHD, this same basic issue has received some attention,[6] but due to the periodic boundary conditions in full PIC the problem was not previously noticed.

For large systems, it appears that the ultimate length of the electron diffusion region is limited by the stability of the thin electron current layer to secondary island production. This mechanism may provide a natural limit on how large the diffusion region D_e can extend which in turn will determine the average reconnection rate. In this scenario, fast reconnection may still be possible provided the generation of secondary islands remains sufficiently vigorous. To confirm this hypothesis for physically relevant regimes, it will be necessary to examine how the stretching process and subsequent island formation scale with m_i/m_e. Although a complete examination of these questions are beyond the scope of this paper, initial results in the following section indicate that the mass ratio dependence of the stretching process is quite weak.

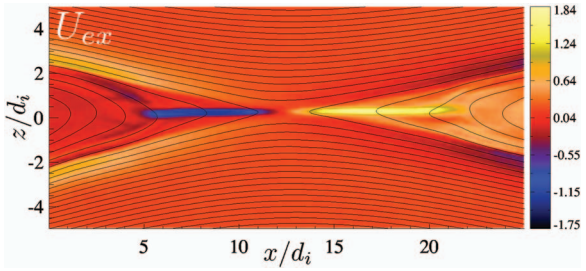

FIG. 17. (Color) Electron outflow velocity U_{ex} for the $m_i/m_e=100$ open boundary simulation at $t\Omega_{ci}=52$. Black lines denote flux surfaces and the box size is $25d_i \times 25d_i$. Initial conditions are the same as the low mass ratio case [see Eq. (19)].

V. DEPENDENCE ON MASS RATIO

To examine the mass ratio dependence of the new results, we consider four open boundary simulations in which the mass ratio is varied by a factor of 100 while all other plasma parameters are held fixed [see Eq. (19)]. These four cases include $m_i/m_e=1$, 6, 25, 100, where the $m_i/m_e=25$ case was already discussed in Sec. III A. The focus is to examine the initial elongation of the electron diffusion region after the onset of reconnection, while the issue of island formation is deferred to a future study. For the $m_i/m_e=1$ case, it was necessary to use a larger domain $50d_i \times 50d_i$ to allow adequate room for expansion of the electron diffusion region over the time interval considered, while the other three cases employed a $25d_i \times 25d_i$ domain. The $m_i/m_e=100$ simulation required 1280×1280 cells and 8×10^8 particles. In each case, the resulting development of the reconnection electric field at the x-point follows a similar pattern. The reconnection rate reaches a maximum and then decreases accompanied by pronounced stretching of the electron diffusion region. The resulting electron outflow velocity is shown for the $m_i/m_e=100$ case in Fig. 17 for a simulation time $t\Omega_{ci}=52$ just past the peak reconnection rate. From a visual inspection, it is clear that the spatial extent of the electron outflow jets for the $m_i/m_e=100$ case is comparable to the $m_i/m_e=25$ case shown in Fig. 8(e), indicating the mass ratio dependence is weak.

To examine these results in more detail, the length of the electron diffusion region was calculated for each case using the method described in Sec. IV. For a given simulation time, the resulting length D_e scales approximately as $(m_e/m_i)^{1/4}$. Thus it is convenient to normalize the results in terms of the dimensionless parameter $D_e^*=(D_e/d_i)(m_i/m_e)^{1/4}$ to organize the data. As shown in the top panel of Fig. 18, the measured length of the electron diffusion region is well described by this scaling over the interval considered. In each case, the length D_e is not measured at early time since the diagnostic is not very meaningful during the onset phase. The observed reconnection electric field at the x-point is shown in the bottom panel of Fig. 18 for each case. In addition, the limiting reconnection rates through the ion and electron diffusion regions are estimated for the $m_i/m_e=100$ case using the method described in Sec. IV. These results demonstrate that the electrons remain the bottleneck controlling reconnection at $m_i/m_e=100$. Furthermore, the weak scaling of D_e with

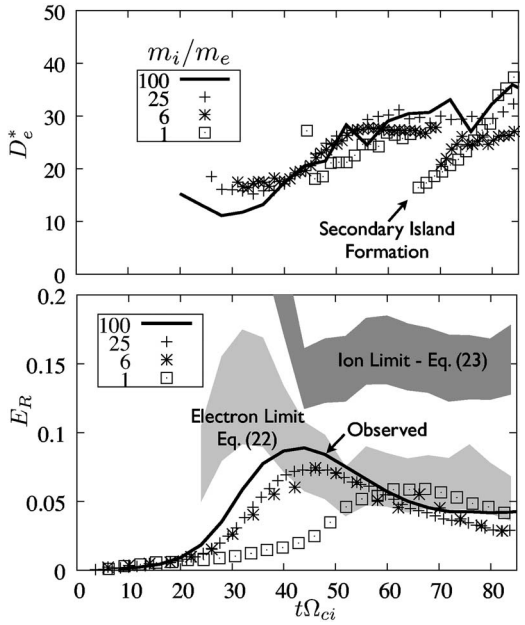

FIG. 18. Length of the electron diffusion region (top) and observed reconnection electric field at the x-point (bottom) from four different open boundary simulations with mass ratio indicated. In the top panel, the length is normalized by $D_e^*=(D_e/d_i)(m_i/m_e)^{1/4}$. The shaded regions correspond to the limiting rates for the $m_i/m_e=100$ case. The electron limit is evaluated from Eq. (22) with $\delta_e/d_e\approx 3\rightarrow 4$ while the ion limit is evaluated from Eq. (23) with $\delta_i/d_i\approx 4\rightarrow 5$.

$(m_e/m_i)^{1/4}$ suggests that meandering electron orbits play a significant role in determining this length. In contrast, the width δ_e measured by the full width at half maximum of $(\mathbf{E}+\mathbf{U}_e\times\mathbf{B})$ scales approximately with $(m_e/m_i)^{1/2}$ indicating the electron skin depth is playing an important role.[31] The density factor in Eq. (22) is essentially the same in all cases, while the upstream magnetic field scales approximately as $(B_{\delta_e}/B_o)^2\propto(m_e/m_i)^{1/8}$. Putting these factors together, the limiting reconnection rate for the inner region in Eq. (22) scales approximately as $E_R\propto(m_i/m_e)^{1/8}$ which is in good agreement with the observed peak reconnection rates in Fig. 18.

It should be emphasized that these scalings only apply to the initial expansion of the diffusion region after the onset of reconnection in a fairly small system. For longer intervals and/or larger systems the formation of secondary islands will complicate the picture and there may be no simple scaling. For example, the decrease in D_e^* at $t\Omega_{ci}\approx 65$ for the $m_i/m_e=1,6$ cases in Fig. 18 corresponds to the formation of small secondary islands. As a consequence, the reconnection rate is modified. The $m_i/m_e=25$ case did not produce a secondary island until $t\Omega_{ci}=95$ while the $m_i/m_e=100$ case did not produce any islands over the interval considered. Thus the formation of secondary islands is clearly sensitive to the mass ratio, but a detailed examination is beyond the scope of this manuscript.

Finally, the limit $m_i=m_e$ deserves special consideration since the Hall term cancels exactly, there are no whistler waves[20] and for $T_i=T_e$ there is only one diffusion region. In this limit, we have performed open boundary simulations with domain sizes as large as $150d_i\times 150d_i$ over durations as long as $t\Omega_{ci}=1000$. The results show stretching of the diffusion region followed by secondary island formation throughout the duration of the simulation (cycle repeated 9 times). The average reconnection rate remain quite fast $E_R\approx 0.08$ even for very large systems. To confirm these results, we have performed periodic simulations with domain sizes as large as $500d_i\times 500d_i$, and the results also show strong stretching of the diffusion region followed by the robust formation of secondary islands. This again demonstrates that the new results are not an artifact of the boundary conditions. Furthermore, these results suggest that the essential physics of reconnection for the $m_i=m_e$ limit may in fact be qualitatively similar to the $m_i/m_e=25$ case already discussed.

VI. SUMMARY

Periodic boundary conditions severely limit the duration in which kinetic simulations of magnetic reconnection are physically meaningful due to the recirculation of particles and the resulting back pressure on the dynamics. The new open boundary model eliminates these artificial effects and allows magnetic flux to enter the system as needed and to freely convect outwards from the x-point. This approach effectively mimics a much larger system and permits the kinetic structure of the reconnection layer to develop over time scales much longer than have ever been simulated with a fully kinetic approach. While at early times the peak reconnection rates are in excellent agreement with previous periodic studies,[29–32] the evolution over longer intervals is entirely different. The essential reason for these new results is that the length of the electron diffusion region D_e does not remain microscopic. Instead, the rapid outward convection of magnetic flux due to the electron jets leads to a reduction in the B_z field, which in turn leads to further expansion of the jets. As a consequence, an extended electron-scale current sheet is formed that periodically becomes unstable to secondary island generation. No pileup of magnetic field is observed, contrary to the MHD models where stretching of the diffusion region is associated with flux pileup. To summarize the major conclusions:

- The length of the electron diffusion region does not remain microscopic, but gradually increases with time to $D_e\sim 25$ d_i for the parameters considered.
- As the length of the electron diffusion region becomes large, the electrons become the bottleneck limiting the reconnection rate.
- Reconnection in a neutral sheet is inherently time-dependent. Fast reconnection may still be possible provided that the generation of secondary islands remains viable for a given parameter regime.
- The dependence of the reconnection dynamics on system size is no longer simple. For small systems, the expansion of the electron diffusion region is limited by the box size and the generation of islands is suppressed. For large systems, the maximum length of the electron diffusion region is limited by the stability of the extended electron current sheet to secondary island formation.
- After the onset of reconnection, the initial expansion of D_e

scales as $(m_e/m_i)^{1/4}$ indicating the mass ratio dependence of the stretching process is weak.

These results are not consistent with the standard model of Hall mediated fast reconnection. Despite evidence that the Hall term plays a role in localizing the diffusion region in fluid simulations,[12,15,16] it does not appear to play the same role in fully kinetic simulations. However, the fluid models contain many uncontrolled approximations. To fully capture the physics reported in this manuscript it appears that fully kinetic simulations may be required. It seems unlikely that hybrid codes[24,27] can properly describe the dynamics but even implicit full PIC codes[32] may miss essential electron physics if the inner layer is not fully resolved.

From these initial open boundary simulations, it appears the maximum length of the electron diffusion region is controlled by the stability of the elongated current sheet. This result suggests a new hypothesis in which fast reconnection may still be possible so long as the process for generating secondary islands remains vigorous for realistic parameter regimes. While the island formation is probably related to an unstable tearing mode, the structure of the electron layer is quite different than a Harris sheet (bifurcated current profile, normal component of **B**, velocity shear, electron anisotropy, etc.) so it is difficult to directly apply previous results. To understand the physical relevance of these new results, future work must clearly address the mass ratio dependence of both the stretching process and the secondary island formation.

Finally, it should be emphasized that all the results in this manuscript are based on 2D simulations which preclude the possibility of plasma instabilities in the out-of-plane direction. Potential driving factors include intense electron streaming, velocity shear, anisotropy, and density gradients. These instabilities may dramatically alter the dynamical evolution of the reconnecting layer, and could potentially play some role in localizing the diffusion region. Thus, to fully understand the physics of collisionless reconnection remains an enormous challenge.

ACKNOWLEDGMENTS

The authors are grateful to D. Krauss-Varban for enlightening discussions regarding this work.

This material is based on work supported by the National Science Foundation under Grant No. 0447423, by NASA under Grants Nos. NNG05GF46G, NNG05GJ25G, and NNG05GC28G, and by a joint UCSD-Los Alamos IGPP grant. Simulations were partially performed at Los Alamos National Laboratory and the San Diego Supercomputer Center, which is supported by the National Science Foundation.

[1] V. Vasyliunas, Rev. Geophys. **13**, 303 (1975).
[2] J. Dungey, Phys. Rev. Lett. **6**, 47 (1961).
[3] M. Ugai and T. Tsuda, J. Plasma Phys. **17**, 337 (1977).
[4] D. Biskamp, Phys. Fluids **29**, 1520 (1986).
[5] M. Yan, L. Lee, and E. Priest, J. Geophys. Res. **92**, 8277 (1992).
[6] D. Uzdensky and R. Kulsrud, Phys. Plasmas **7**, 4018 (2000).
[7] N. Erkaev, V. Semenov, and F. Jamitzky, Phys. Rev. Lett. **84**, 1455 (2000).
[8] D. Biskamp and E. Schwarz, Phys. Plasmas **8**, 4729 (2001).
[9] M. Mandt, R. Denton, and J. Drake, Geophys. Res. Lett. **21**, 73 (1994).
[10] D. Biskamp, E. Schwarz, and J. Drake, Phys. Plasmas **4**, 1002 (1997).
[11] M. Shay and J. Drake, Geophys. Res. Lett. **25**, 3759 (1998).
[12] M. Shay, J. Drake, and B. Rogers, Geophys. Res. Lett. **26**, 2163 (1999).
[13] B. Rogers, R. Denton, J. Drake, and M. Shay, Phys. Rev. Lett. **87**, 195004 (2001).
[14] J. Birn, J. Drake, M. Shay, B. Rogers, R. Denton, M. Hesse, M. Kuznetsova, Z. Ma, A. Bhattacharjee, A. Otto *et al.*, J. Geophys. Res. **106**, 3715 (2001).
[15] M. Shay, J. Drake, and M. Swisdak, Phys. Plasmas **11**, 2199 (2004).
[16] J. Huba and L. Rudakov, Phys. Rev. Lett. **93**, 175003 (2004).
[17] X. Wang, A. Bhattacharjee, and Z. Ma, Phys. Rev. Lett. **87**, 265003 (2001).
[18] R. Fitzpatrick, Phys. Plasmas **11**, 937 (2004).
[19] H. Karimabadi, D. Krauss-Varban, J. Huba, and H. Vu, J. Geophys. Res. **109**, A09205 (2004).
[20] N. Bessho and A. Bhattacharjee, Phys. Rev. Lett. **95**, 245001 (2005).
[21] M. Scholer, J. Geophys. Res. **94**, 8805 (1989).
[22] W. Matthaeus and D. Montgomery, J. Plasma Phys. **25**, 11 (1981).
[23] L. Lee and Z. Fu, J. Geophys. Res. **91**, 3311 (1986).
[24] M. Shay, J. Drake, R. Denton, and D. Biskamp, J. Geophys. Res. **103**, 9165 (1998).
[25] D. Krauss-Varban, H. Karimabadi, and N. Omidi, Geophys. Res. Lett. **26**, 1235 (1999).
[26] L. Yin, D. Winske, S. Gary, and J. Birn, J. Geophys. Res. **106**, 10,761 (2001).
[27] H. Karimabadi, W. Daughton, and K. Quest, J. Geophys. Res. **110**, A03213 (2005).
[28] R. Horiuchi, W. Pei, and T. Sato, Earth, Planets Space **53**, 439 (2001).
[29] P. Pritchett, J. Geophys. Res. **106**, 3783 (2001).
[30] M. Hesse, J. Birn, and M. Kuznetsova, J. Geophys. Res. **106**, 3721 (2001).
[31] M. Shay, J. Drake, B. Rogers, and R. Denton, J. Geophys. Res. **106**, 3759 (2001).
[32] P. Ricci, G. Lapenta, and J. Brackbill, Geophys. Res. Lett. **29**, 2088 (2002).
[33] J. Huba, Phys. Plasmas **12**, 012322 (2005).
[34] D. Krauss-Varban and N. Omidi, Geophys. Res. Lett. **22**, 3271 (1995).
[35] H. Karimabadi, D. Krauss-Varban, N. Omidi, and H. X. Vu, J. Geophys. Res. **104**, 12313 (1999).
[36] D. Ding, L. Lee, and D. Swift, J. Geophys. Res. **97**, 8453 (1992).
[37] R. Horiuchi and T. Sato, Phys. Plasmas **4**, 277 (1997).
[38] W. Pei, R. Horiuchi, and T. Sato, Phys. Rev. Lett. **87**, 235003 (2001).
[39] W. Pei, R. Horiuchi, and T. Sato, Phys. Plasmas **8**, 3251 (2001).
[40] A. Ishizawa, R. Horiuchi, and H. Ohtani, Phys. Plasmas **11**, 3579 (2004).
[41] A. Ishizawa, R. Horiuchi, and H. Ohtani, Phys. Rev. Lett. **94**, 045003 (2005).
[42] P. Pritchett, J. Geophys. Res. **110**, A05209 (2005).
[43] W. Daughton, Phys. Plasmas **9**, 3668 (2002).
[44] W. Daughton, Phys. Plasmas **10**, 3103 (2003).
[45] W. Daughton, P. Ricci, and P. Ricci, Phys. Rev. Lett. **93**, 105004 (2004).
[46] P. Ricci, J. Brackbill, W. Daughton, and G. Lapenta, Phys. Plasmas **11**, 4489 (2004).
[47] R. Morse and C. Nielson, Phys. Fluids **14**, 830 (1971).
[48] D. Forslund, in *Space Plasma Simulations*, edited by M. Ashour-Abdalla and D. Dutton (Reidel, Norwell, 1985), pp. 425–439.
[49] T. Forbes and E. Priest, Rev. Geophys. **25**, 1583 (1987).
[50] C. Birdsall and A. Langdon, *Plasma Physics via Computer Simulation* (McGraw-Hill, New York, 1985).
[51] C. Nielson and E. Lindman, presented at the 6th Conference on Numerical Simulation of Plasmas, sponsored by Lawrence Livermore Laboratory, held at Lawrence Berkeley Laboratory, Berkeley, California (1972).
[52] E. Lindman, J. Comput. Phys. **18**, 66 (1975).
[53] J. Berenger, J. Comput. Phys. **114**, 185 (1994).
[54] E. G. Harris, Nuovo Cimento **23**, 115 (1962).
[55] P. Ricci, J. Brackbill, W. Daughton, and G. Lapenta, Phys. Plasmas **11**, 4102 (2004).